ADVANCED MATERIALS
www.advmat.de

Light-Induced Giant Rashba Spin–Orbit Coupling at Superconducting $KTaO_3$(110) Heterointerfaces

Yulin Gan, Fazhi Yang, Lingyuan Kong, Xuejiao Chen, Hao Xu, Jin Zhao, Gang Li, Yuchen Zhao, Lei Yan, Zhicheng Zhong, Yunzhong Chen,* and Hong Ding**

The 2D electron system (2DES) at the $KTaO_3$ surface or heterointerface with 5d orbitals hosts extraordinary physical properties, including a stronger Rashba spin–orbit coupling (RSOC), higher superconducting transition temperature, and potential of topological superconductivity. Herein, a huge enhancement of RSOC under light illumination achieved at a superconducting amorphous-$Hf_{0.5}Zr_{0.5}O_2$/$KTaO_3$(110) heterointerface is reported. The superconducting transition is observed with $T_c = 0.62$ K and the temperature-dependent upper critical field reveals the interaction between spin–orbit scattering and superconductivity. A strong RSOC with $B_{so} = 1.9$ T is revealed by weak antilocalization in the normal state, which undergoes sevenfold enhancement under light illumination. Furthermore, RSOC strength develops a dome-shaped dependence of carrier density with the maximum of $B_{so} = 12.6$ T achieved near the Lifshitz transition point $n_c \approx 4.1 \times 10^{13}$ cm^{-2}. The highly tunable giant RSOC at $KTaO_3$(110)-based superconducting interfaces show great potential for spintronics.

1. Introduction

Antisymmetric spin–orbit coupling (SOC) could guarantee spin-momentum locking of the charge carrier and allow the manipulation of spin rotation, which plays a key role in the development of future quantum electronic/spintronic devices.[1,2] Currently, the broken structural inversion symmetry at surfaces or interfaces becomes the heart of the growing research field of spintronics[3,4] and has been extensively investigated in various systems including semiconductors,[5,6] topological insulators,[7] and complex oxide interfaces.[8] Among them, the strong Rashba spin–orbit coupling (RSOC) of 2D electron system (2DES) trapped at complex oxide surfaces or interfaces allows the electric or light gating modulation,[8,9] and enables a highly efficient spin-to-charge conversion,[10] providing an energetically competitive candidate for the development of spintronic logic devices.[11]

The burgeoning 2DESs at surfaces or interfaces of complex oxides, the prime example of which is the $LaAlO_3$/$SrTiO_3$ (LAO/STO) interfaces, not only show strong RSOC but also possess diverse emergent properties and functionalities, such as superconductivity (SC)[12,13] and ferromagnetism.[14] Their coexistence or interaction[15,16] promotes emergent electronic states that favor the control of novel quantum orders for potential applications. It's worth noting that the RSOC would lead to spin-split parabolic interfacial states and form helical spin texture on the Fermi contours, showing a topologically nontrivial electronic state. The combination of SC and RSOC is predicted to generate topological superconductivity.[17] Therefore, oxide 2DESs hosting both SC and strong RSOC are also ideal systems to search for topological superconductors and related applications.[18,19]

The RSOC induced an effective magnetic field B_{so} determines the spin precession and degeneration. A large RSOC and its enhancement have been widely pursued for 3d 2DESs at STO-based interfaces. Despite the discovery of the interesting correlation between RSOC and SC, both the SC transition temperature ($T_c <$ 0.3 K) and the spin–orbit energy ($E_{so} = 0.01$–0.04 meV) at STO-based interfaces remain low. Compared to the 3d 2DESs, the 5d 2DESs at $KTaO_3$(KTO)-based interfaces have been found to host both stronger RSOC (B_{so} up to 2.6 T and E_{so} as high as 0.2 meV for (001)-oriented interfaces)[20] and higher SC transition temperature (T_c up to 2.2 K for (111)-oriented interfaces).[21–23]

Y. Gan, F. Yang, L. Kong[+], H. Xu, J. Zhao, G. Li, Y. Zhao, L. Yan, Y. Chen, H. Ding
Beijing National Laboratory of Condensed Matter Physics and Institute of Physics
Chinese Academy of Sciences
Beijing 100190, China
E-mail: yzchen@iphy.ac.cn; dingh@sjtu.edu.cn

X. Chen, Z. Zhong
Key Laboratory of Magnetic Materials and Devices and Zhejiang Province Key Laboratory of Magnetic Materials and Application Technology
Ningbo Institute of Materials Technology and Engineering (NIMTE)
Chinese Academy of Sciences
Ningbo 315201, China
E-mail: zhong@nimte.ac.cn

H. Ding
Tsung-Dao Lee Institute & School of Physics and Astronomy
Shanghai Jiao Tong University
Shanghai 200240, China

H. Ding
CAS Center for Excellence in Topological Quantum Computation
University of Chinese Academy of Sciences
Beijing 100190, China

The ORCID identification number(s) for the author(s) of this article can be found under https://doi.org/10.1002/adma.202300582

[+]Present address: T. J. Watson Laboratory of Applied Physics & Institute for Quantum Information and Matter, California Institute of Technology, Pasadena, CA91125, USA

DOI: 10.1002/adma.202300582

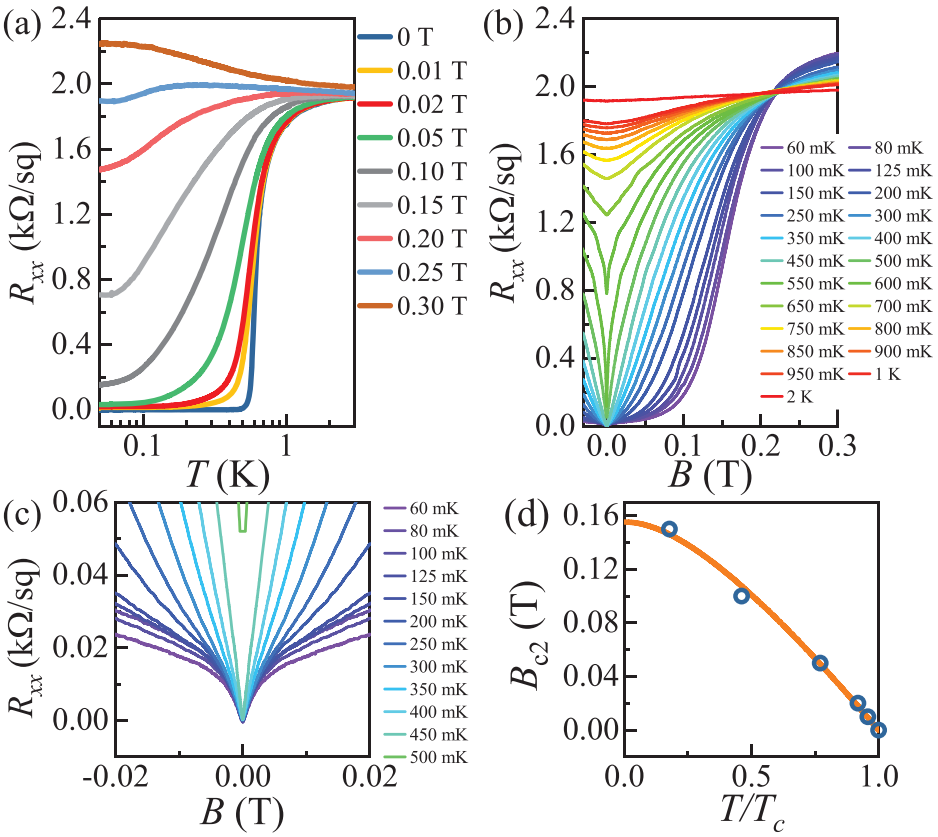

Figure 1. a) Temperature-dependent R_{xx} for various out-of-plane B. b) The out-of-plane B dependence of R_{xx} at different temperatures. c) A zoom-in of the anomalous metallic state at low field observed in superconducting regime. d) Temperature dependence of B_{c2} derived from the midpoint. The orange solid line represents the best fit from the WHH model.

Meanwhile, the anisotropic 2DESs along different orientations[24] and interfacial strong correlations[25] could offer high flexibility to engineer their properties, presenting a valuable platform for not only energy-efficient spintronic devices but also the coexistence of RSOC and SC. However, to date, the RSOC of 5d 2DESs has been investigated exclusively at KTO (001) interfaces without SC, and the RSOC at superconducting KTO (110) or (111) interface was rarely investigated.[26,27]

In this work, we achieved a very large RSOC at a superconducting $Hf_{0.5}Zr_{0.5}O_2/KTaO_3$(110) heterostructure grown at room temperature. The typical superconducting transition is observed at $T_c \approx 0.62$ K. Meanwhile, the investigation of weak antilocalization (WAL) suggests a giant RSOC in this system. Further light-gating modulates the band filling, which reveals a dome-shaped dependence of RSOC on carrier density (n_{tot}) with B_{so} enhanced seven times around the Lifshitz transition point. Such highly tunable giant RSOC in a superconductor should promote endeavors to the development of spin field-effect transistor and exploration of topologically nontrivial electronic states.

2. Results and Discussion

2.1. Superconductivity

The 12 nm amorphous $Hf_{0.5}Zr_{0.5}O_2$ (a-HZO) films with Hall bar geometry were deposited on KTO (110) single-crystal substrates at room temperature at the base pressure of $\approx 1 \times 10^{-7}$ mbar by pulsed laser deposition (PLD). The temperature-dependent sheet resistance R_{xx} (R_{xx}–T) of a-HZO/KTO (110) interface (Figure S3a, Supporting Information) shows a clear superconducting transition at midpoint $T_c = 0.62$ K, which can be well described by the Berezinskii–Kosterlitz–Thouless (BKT) model[12] for a 2D superconducting system, giving a T_{BKT} of ≈0.593 K (Figure S3b, Supporting Information). By increasing out-of-plane magnetic field B, the superconducting transition is fully suppressed when $B \geq 0.3$ T, showing a superconductor–metal transition with the critical R_{xx} around 2 kΩ sq^{-1} (**Figure 1**a). Interestingly, a low field as small as 0.01 T could break the zero resistance, and a finite residual R_{xx} (≈ 15.4 Ω sq^{-1}) at low temperatures following the sharp resistance drop is observed, indicating an anomalous metallic state.[28] Such saturated residual resistance grows as B increases. The further magnetoresistance isotherms in Figure 1b exhibit an anomalous magnetoresistance at low field (a zoom-in image in Figure 1c), which is superimposed on the typical U-shaped magnetoresistance derived from the B-induced superconducting transition and may relate to the RSOC[15,26] as discussed in detail later. The presence of SOC in SC has an impact on upper critical field B_{c2}, where the Werthamer–Helfand–Hohenberg (WHH) model incorporating the spin-paramagnetic and spin–orbit scattering terms was developed to describe the behavior of T-dependent B_{c2} (Figure 1d)[29] (Section S2, Supporting Information). The fitted dimensionless $\lambda_{so} = 0.609$ mirrors

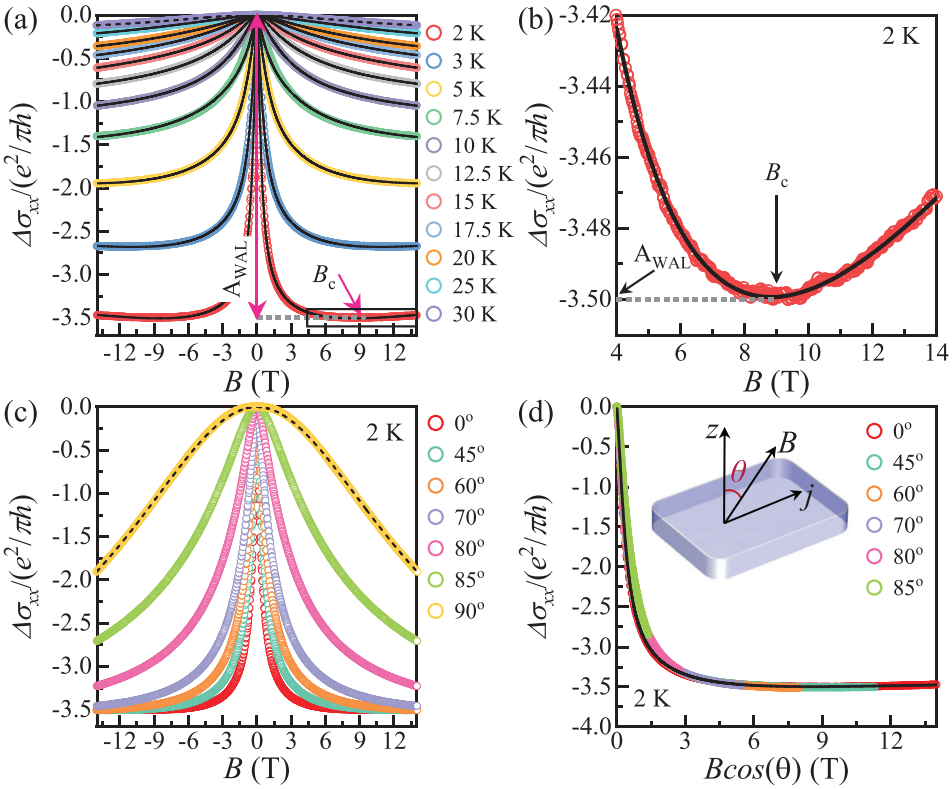

Figure 2. a) The MC from 2 to 30 K. The A_{WAL} and B_c characterize the phase-coherent transport and RSOC. b) A zoom-in of the black rectangle region in (a) shows a pronounced B-induced WAL-WL transition, which forms a minimum at B_c. c) The MC in tilted B fields at 2 K. The short-dashed curve is the best fit of OMC to Kohler's rule. d) MC as a function of Bcosθ. Inset: Schematic drawing of the device in tilted B. Solid curves are the best fits of the MC to MF model.

the non-negligible interaction between SC and the spin–orbit scattering.[30]

2.2. A Large Rashba Spin–Orbit Coupling of 5d Electrons

Besides SC, the WAL phenomenon is another powerful way to characterize the interfacial RSOC. The magnetoconductance (MC) measurements with out-of-plane B in the normal states are performed to detect the RSOC strength. In **Figure 2**a, the MC at 2 K first decrease rapidly to a minimum at a critical field (B_c) forming a negative cusp-shaped MC with a maximum at $B = 0$ followed by an increasing MC, showing a WAL behavior in typical weak localization (WL) system. Here, both the phase-coherent transport and RSOC contribute to the WAL, which are mainly determined by the inelastic scattering field (B_i) and B_{so}, respectively. These negative and positive MC behaviors are attributed to the dominant WAL and WL regimes, respectively. Therefore, the B_c in Figure 2b signifies the B-induced crossover from WAL ($B < B_c$) to WL ($B_c < B$) and approximately reflects the RSOC strength, i.e., $B_{so} \propto B_c$.[31,32] Meanwhile, the WAL amplitude (A_{WAL}), i.e., the absolute value of $\Delta\sigma_{xx}$ at B_c, reflects the interaction between RSOC and WL, so it is proportional to B_{so}/B_i.[33] Compared with general STO-based interfaces ($A_{WAL} < e^2/\pi h$ and $B_c <$ 5T)[8,9,31,32,34] and other representative families ($A_{WAL} < 0.5e^2/\pi h$ and $B_c < 0.5$T),[6,35–38] the WAL in our a-HZO/KTO (110) interface at 2 K shows much larger A_{WAL} (up to $3.5e^2/\pi h$) and higher B_c (up to ≈9 T), suggesting a very large RSOC.

Upon warming in Figure 2a, the WAL is broadened and disappears above 30 K due to decreasing WL.[7] Here, the negative MC at 30 K primarily shows a quadratic B dependence (Figure S4, Supporting Information), which originates from the orbital effects related ordinary MC (OMC). Therefore, the total MC is mainly contributed from both the WAL and OMC. Normally, OMC obeys the Kohler's rule and becomes stronger with increasing mobility.[39] Here, the mobility ($\mu_{tot} = 1/(en_{tot}R_{xx}(0))$ (Figure S5, Supporting Information) increases by approximately an order of magnitude from 10 cm^2 V^{-1} s^{-1} at 300 K to 136 cm^2 V^{-1} s^{-1} at 2 K, thereby the OMC should become stronger at lower temperature. However, the OMC is surpassed by WAL totally up to 14 T at 2 K (Figure 2b), suggesting a strong WAL and implying a very large RSOC effect again. With increasing temperature, the OMC appears gradually at high field and dominates the MC above 30 K completely.

For typical RSOC from the interfacial breaking of inversion symmetry, the electron spin should be confined at the interface, which would compete with the in-plane B ($B_{||}$) induced Zeeman effect.[40] The WAL effect is further investigated in tilted B and becomes broader with increasing relative angle (θ) between B and the out-of-plane direction (Figure 2c). When B is tilted parallel to the interface ($\theta = 90°$), the WAL induced cusp-shaped MC feature disappears completely, only leaving behind the OMC. When

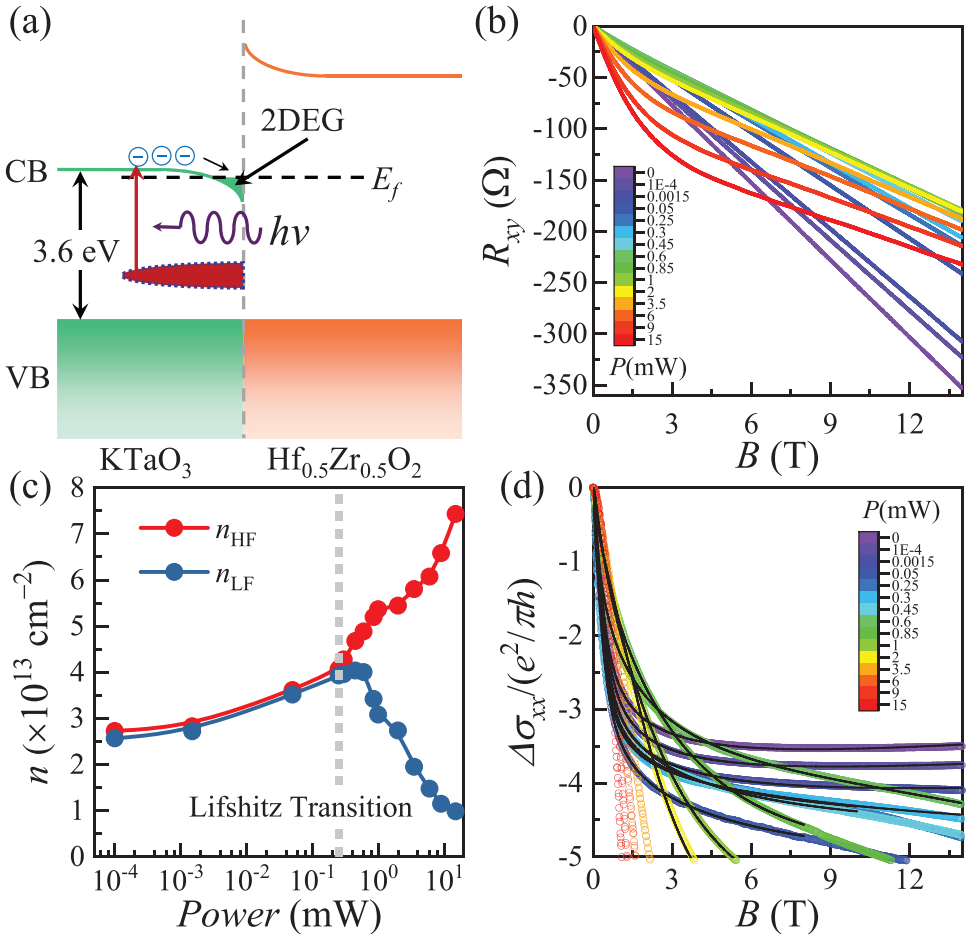

Figure 3. a) Schematic of the light-gating mechanism. b) The evolution of Hall effect for increasing laser power. c) The n_{LF} and n_{HF} as a function of laser power. d) The evolution of MC with increasing laser power. The solid black curves are the best fits to MF model.

presented as a function of the perpendicular component of B, i.e., $B\cos\theta$, all MC curves in Figure 2d coincide with each other for the entire field range. Meanwhile, the absence of significant suppression of WAL from Zeeman-type spin splitting up to 14 T also implies a very large RSOC,[7] where the $\Delta_{so} >> \sqrt{2\mu_B B_{\parallel} e\hbar/\mu_{tot} m^*} \approx 6$ meV ($m^* = 0.36m_e$ is the effective mass[20]).

To quantify RSOC strength, the 2D localization theory in diffusion regime developed by Maekawa–Fukuyama (MF) with the D'yakonov–Perel mechanism of spin relaxation is employed to analyze the WAL induced quantum correction on MC.[8,31] The total MC is expressed as:

$$\frac{\Delta\sigma_{xx}(B)}{G_0} = \psi\left(\frac{1}{2}+\frac{B_i+B_{so}}{B}\right)+\frac{1}{2}\psi\left(\frac{1}{2}+\frac{B_i+2B_{so}}{B}\right) -\frac{1}{2}\psi\left(\frac{1}{2}+\frac{B_i}{B}\right)-\left[\ln\left(\frac{B_i+B_{so}}{B}\right) +\frac{1}{2}\ln\left(\frac{B_i+2B_{so}}{B_i}\right)\right]-A_k\frac{\sigma_{xx}(0)}{G_0}\frac{B^2}{1+CB^2} \quad (1)$$

where $\psi(x)$ is the digamma function and $G_0 = e^2/(\pi h)$. The last term from Kohler's rule describes the OMC with fitting parameters A_k and C. The best fit at 2 K extracts the B_{so} of 1.9 T, which is approximately $B_c/4 \approx 2.25$ T,[5,32] and the deduced spin splitting energy $\Delta_{so} = 2\alpha_R k_F = 28.4$ meV[35,41] ($\alpha_R = \sqrt{e\hbar^3 B_{so}}/m^*$ is the Rashba coefficient and $k_F = \sqrt{2\pi n_{tot}}$). This is indeed much stronger than the 6 meV evaluated by the in-plane Zeeman effect. With warming, the spin relaxation time extracted from the best fits of temperature-dependent MC to MF model is inversely proportional to relaxation time, showing consistency with the D'yakonov–Perel mechanism of spin relaxation[6,8] (Figure S4, Supporting Information). Meanwhile, the increasing B_i reveals a weakened WL, showing good agreement with the broadened WAL.

2.3. Light-Induced Enhancement of Rashba Spin–Orbit Coupling

To further modulate such RSOC, light gating experiments with the laser wavelength of 375 nm (≈3.306 eV) are carried out to increase the n_{tot} by pumping the electrons localized at the in-gap states to the Ta 5d t_{2g} conducting bands (**Figure 3**a).[20] By controlling the laser power (P) up to 15 mW, the Hall effect undergoes a linear to nonlinear transition when $P > 0.25$ mW (Figure 3b). The nonlinear Hall effects show a linear B-dependence at low field

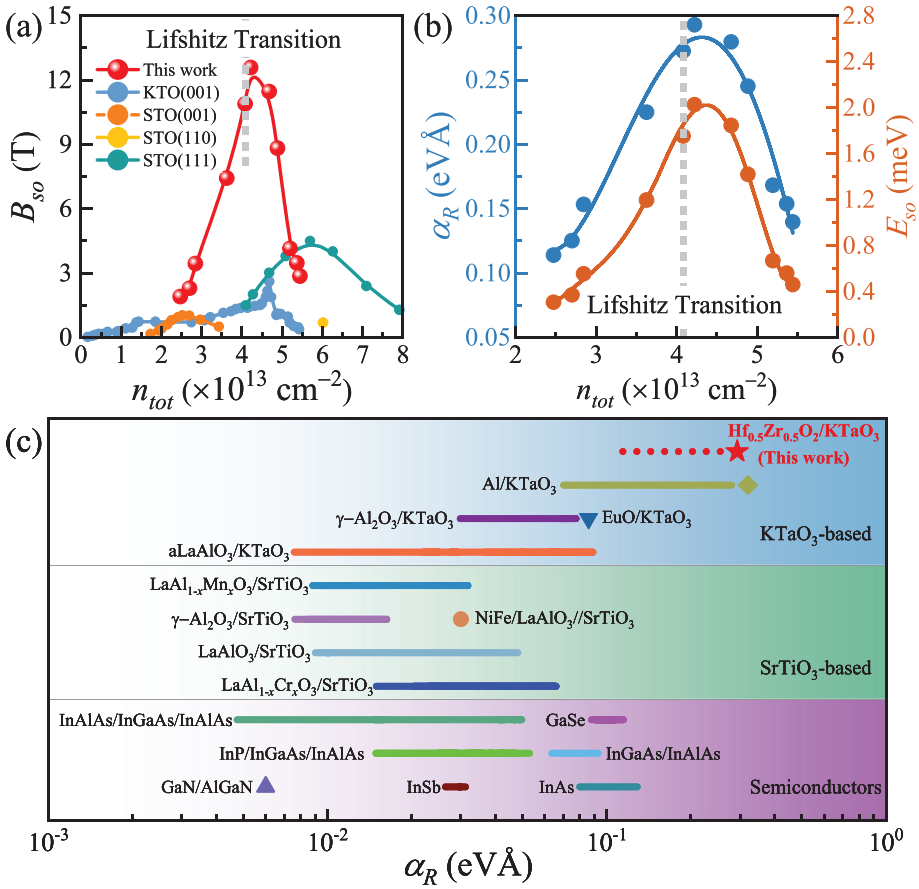

Figure 4. a) Comparison of B_{so} among different RSOC systems (KTO(001),[20] STO(001),[9] STO(110),[46] STO(111).[47] The B_{so} in this work is extracted from the best fits in Figure 3d. b) The α_R and E_{so} as a function of carrier density. c) Comparative graph of Rashba coefficients mainly extracted from the transport measurements of various mainstream 2DESs for low-power spintronics, including KTO-based systems (Al/$KTaO_3$ with *g*-factor of 0.5–2,[48] and the related value extracted from ARPES is marked as rhombus,[56] γ-$Al_2O_3/KTaO_3$,[44] EuO/$KTaO_3$,[49] aLaAlO$_3$/$KTaO_3$[20]), STO-based systems ($LaAl_{1-x}Mn_xO_3/SrTiO_3$ ($0 \le x \le 1$),[31] γ-$Al_2O_3/SrTiO_3$,[34] $LaAlO_3/SrTiO_3$,[8] $LaAl_{1-x}Cr_xO_3/SrTiO_3$ ($x = 0,0.1,0.2$),[50] NiFe/LAO//STO[10]) and semiconductors (InAlAs/InGaAs/InAlAs,[35] GaSe,[41] InP/InGaAs/InAlAs,[51] InGaAs/InAlAs,[52] GaN/AlGaN,[53] InSb,[37] InAs[54]).

and then change to nonlinear *B*-dependence at high field, forming an anticlockwise bending, which is a typical behavior of ordinary Hall effect contributed by two types of carriers, and the critical carrier density (n_c) at the transition point implies the Lifshtz transition of the energy band structure.[42,43] Therefore, the two-carrier model (Figure S6, Supporting Information) is employed to extract the carrier density from the Hall coefficients ($R_h = dR_{xy}/dB$) at $B \approx 0$ T and 14 T, where the $n_{LF} = 1/(-eR_h(B \to 0))$ and $n_{HF} = 1/(-eR_h(B \to \infty))$ give the carrier density of electrons with higher mobility and n_{tot}, respectively.[42] An obvious divergence between n_{LF} and n_{HF} is observed for $P > 0.25$ mW in Figure 3c, indicating the Lifshitz transition at n_c of $\approx 4.1 \times 10^{13}$ cm^{-2}. With the monotonous increase of n_{tot} from 2.5×10^{13} to 7.4×10^{13} cm^{-2}, the $R_{xx}(0)$ in Figure S7a (Supporting Information) undergoes a similar evolution with previous reports on optical modulation of 2DESs at KTO(001)-based interfaces.[20,44] As n_{tot} increases, the MC in Figure 3d transits gradually from a typical WAL behavior at 0 mW to a typical two-carrier induced OMC with undetectable WAL contribution at 15 mW (Figure S8, Supporting Information), where the RSOC is highly tuned (Figure S9, Supporting Information). Notably, analogous to the nonmonotonic evolution of RSOC at STO-based interfaces,[31,32,45] the extracted B_{so} in Figure 3d also exhibit a characteristic dome-shaped dependence on n_{tot} with a maximum of 12.6 T around the Lifshitz transition point in **Figure 4**a. It is worth mentioning that such giant RSOC at a-HZO/KTO interface is significantly stronger than that in other oxide systems,[9,20,46,47] and leads to technologically more competitive α_R = 0.11–0.29 eV Å (Figure 4b,c) than various mainstream 2DESs[8,10,20,31,34,35,37,41,44,48–54] for low-power spintronic devices such as the spin field-effect transistor proposed by Datta and Das[55] where the high α_R leads to high charge–spin conversion efficiency and short gate length ($L = \pi\hbar^2/2\alpha_R m^* = 11.4$–$29.2$ nm) for the shift between the two spin components. The highest Rashba coefficient is similar to the significant spin splitting of band structure with $\alpha_R = 0.32$ eVÅ extracted from the angle-resolved photoemission spectroscopy (ARPES) in (001).[56] (The corresponding Δ_{so} are in Figure S10, Supporting Information.)

A remarkable correlation between RSOC and SC is that the RSOC can convert an *s*-wave superconductor into an effective topological superconductor.[17] The RSOC removes the spin degeneracy of the parabolic energy band and forms two

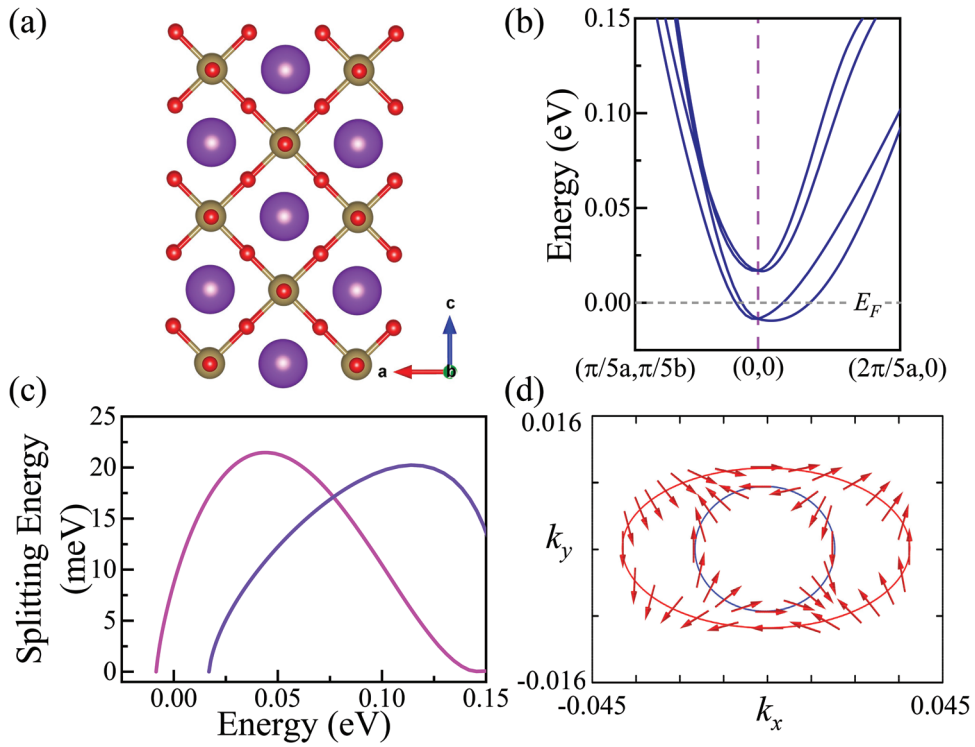

Figure 5. a) The ideal 5-layer slab structure of (110) $KTaO_3$. b) The tight-binding calculated electronic band structure (rigid shift of Fermi level) and the E_F shows the initial Fermi level. c) The splitting energy as a function of energy for the G (0,0) to X ($\frac{\pi}{a}$, 0) k -path for bottom bands 1-2 (magenta line) and 3-4 (violet line) of b). d) Schematic spin-texture at the enlarged region close to the G center based on DFT calculated spin directions (k vector unit: ($\frac{\pi}{a}$, $\frac{\pi}{b}$)).

spin-resolved parabolas, while the displaced energy is $E_{so} = m^*\alpha_R^2/2\hbar^2$and is related to the parameter window of topological phase in a Majorana host. Previous studies on 3d 2DESs in LAO/STO observed zero-bias conductance peaks[19] and e^2/h-quantized conductance plateau,[18] which indicate the precursor of topological superconductivity at oxide heterointerfaces. The E_{so} of 0.31–2.03 meV in a-HZO/KTO (Figure 4b; Table S1, Supporting Information) is much higher than the one in STO-based systems and comparable to that in typical material InAs nanowires.[57] The designer interface is flexible to incorporate a ferromagnet,[43,58] by this way, it is possible to introduce a sufficiently large Dirac gap to the Rashba states, but without destroying the superconductivity.[59] In this view, the a-HZO/KTO heterointerface is potentially promising for topological superconductivity.

2.4. Density Functional Theory Calculations

To further understand the nature of such giant RSOC, we performed density functional theory (DFT) calculations on KTO-based bulk and (110) layered structures. The polar atomic layer sequence of this film and surface symmetry breaking introduce potential divergence to cause electronic and atomic reconstruction. Meantime, specific amorphous HZO interface configurations further tune interfacial electronic structure of the 2DES. In order to capture intrinsic inversion symmetry breaking, we constructed a simple tight-binding model based on bulk Ta-d and O-p orbital projected Wannier basis. Non-symmetry surface lattice is shown in **Figure 5**a, where vertical direction cutting-off causes inversion symmetry breaking of hopping matrix of tight-binding Hamiltonian. Furthermore, the magnitude of atomic spin–orbit coupling forheavy Ta element is much larger than that of 3d transition metal Ti.[60] Rashba-like spin splitting is observed in the tight-binding calculated electronic band structure in Figure 5b due to strong hybridization between Ta-d and O-p orbital. Meantime, light-controlled electron doping shifts realistic Fermi level to cross additional Ta-t_{2g} conduction bands, which make contributions to transport signal. Energy splitting between the up and down parabolic band at Γ high symmetry point is up to 30 meV, corresponding to Lifshitz transition shown in Figure 5b. Inversion symmetry breaking and strong SOC cause spin splitting bands for the lowest four bands, where the splitting energy is presented in Figure 5c with maximum of 20 meV. The estimated α_R (≈0.1 eVÅ) is around one order higher than that (≈10^{-2} eVÅ) in STO systems.[45] Moreover, we use this simple Wannier orbital projected tight-binding model to illustrate the complex Rashba-like spin-texture surface state of (110) perovskite thin film (Figure 5d) based on DFT spin directions, whose relaxed lattice and band structures are presented in (Figure S11, Supporting Information). More interestingly, the spin-texture of KTO might present novel patterns, which is demonstrated by (111)[61] and (001)[62] orientation of KTO slab, combination between linear and cubic term,[63] as well as anomalous hall conductivity with the special spin-texture.[64] These unique spin-orientation features may be rooted in strong SOC, multiplied bands of t_{2g} orbitals,

geometry configuration mixing of different directions of films, and sensitivity of surface or interface, where spin-splitting bands are always observed but unique spin-textures are also presented named as Rashba-like spin-texture.[65]

3. Conclusion

We have created a new oxide heterointerface a-HZO/KTO (110) with both large RSOC (B_{so} = 1.9 T) and superconductivity ($T_c \approx$ 0.62 K). Further light modulation of WAL reveals a giant RSOC, which exhibits a dome-shaped evolution as a function of carrier density. A maximum value of B_{so} = 12.6 T is achieved around the Lifshitz transition point n_c of $\approx 4.1 \times 10^{13}$ cm^{-2}. The giant RSOC, relatively high T_c and large E_{so} ($\approx$0.31–2.03 meV) of our a-HZO/KTO (110) make such system a highly promising candidate for not only energy-efficient spintronic devices but also the exploration of fundamental physics such as topological superconductor in 2DES and non-Abelian braiding statistics in the future.

4. Experimental Section

Sample Fabrication: All samples were grown by pulsed laser deposition (PLD) using a KrF laser on 5 × 5 × 0.5 mm (110) KTO single-crystal substrates. A pulse laser (with a wavelength of 248 nm, a repetition frequency of 2 Hz, and laser fluence of $\approx$1 J cm^{-2}) was focused with a lens onto the $Hf_{0.5}Zr_{0.5}O_2$ ceramic targets. Before film growth, a hard mask made from amorphous $LaMnO_3$ was pre-patterned as the Hall bar geometry by optical lithography (W = 50 µm, L = 500 µm). The 12 nm amorphous $Hf_{0.5}Zr_{0.5}O_2$ films were deposited at room temperature with base pressure of $\approx 1 \times 10^{-7}$ mbar and the distance between target and substrate of $\approx$70 mm. The film thickness and growth rate are calibrated by small-angle X-ray reflectivity (XRR) measurements in Figure S1 (Supporting Information).

Transport Characterization: Both magneto-transport and superconductivity were characterized in the Hall Bar geometry with ultrasonically wire-bonded aluminum wires as electrodes. A commercial physical property measurement system (PPMS, Quantum Design) was employed to characterize the angle-dependent magneto-transport and the light-tunable magneto-transport at low temperatures. A semiconductor laser (λ = 375 nm) was introduced into PPMS by an optical fiber to illuminate the devices and the spot size of the light on devices is $\approx$2 mm in diameter. The laser power (0–15 mW) and photon flux (0–9.01×10^{17} cm^{-2} s^{-1}) are calibrated at the end of the optical fiber. A dilution refrigerator insert with a base temperature of 50 mK in PPMS was used for measuring the superconductivity with perpendicular magnetic field.

Supporting Information

Supporting Information is available from the Wiley Online Library or from the author.

Acknowledgements

The authors thank Yi Liu and Jian Wang for helpful discussion. Project supported by National Natural Science Foundation of China (No.11888101, 52088101, 51327806, 12204523), the Strategic Priority Research Program of Chinese Academy of Sciences (No. XDB28000000, XDB07000000), the National Key Research and Development Program of China (2021YFA1400300), the Key Research Program of Frontier Sciences of CAS (Grant No. ZDBS-LY-SLH008), the China Postdoctoral Science Foundation (2020M680726, YJ20200325). This work was supported by the Synergetic Extreme Condition User Facility (SECUF).

Conflict of Interest

The authors declare no conflict of interest.

Data Availability Statement

The data that support the findings of this study are available from the corresponding author upon reasonable request.

Keywords

oxide interfaces, Rashba spin–orbit coupling, superconductivity, light modulation, Lifshitz transition

Received: January 18, 2023
Revised: March 7, 2023
Published online: May 14, 2023

[1] A. Manchon, H. C. Koo, J. Nitta, S. M. Frolov, R. A. Duine, *Nat. Mater.* **2015**, *14*, 871.
[2] X. Lin, W. Yang, K. L. Wang, W. Zhao, *Nat. Electron.* **2019**, *2*, 274.
[3] A. Soumyanarayanan, N. Reyren, A. Fert, C. Panagopoulos, *Nature* **2016**, *539*, 509.
[4] F. Trier, P. Noël, J.-V. Kim, J.-P. Attané, L. Vila, M. Bibes, *Nat. Rev. Mater.* **2022**, *7*, 258.
[5] P. D. Dresselhaus, C. M. A. Papavassiliou, R. G. Wheeler, R. N. Sacks, *Phys. Rev. Lett.* **1992**, *68*, 106.
[6] C. Niu, G. Qiu, Y. Wang, Z. Zhang, M. Si, W. Wu, P. D. Ye, *Phys. Rev. B* **2020**, *101*, 205414.
[7] H. He, G. Wang, T. Zhang, I.-K. Sou, G. K. L. Wong, J. Wang, H.-Z. Lu, S.-Q. Shen, F.-C. Zhang, *Phys. Rev. Lett.* **2011**, *106*, 166805.
[8] A. D. Caviglia, M. Gabay, S. Gariglio, N. Reyren, C. Cancellieri, J.-M. Triscone, *Phys. Rev. Lett.* **2010**, *104*, 126803.
[9] L. Cheng, L. Wei, H. Liang, Y. Yan, G. Cheng, M. Lv, T. Lin, T. Kang, G. Yu, J. Chu, Z. Zhang, C. Zeng, *Nano Lett.* **2017**, *17*, 6534.
[10] E. Lesne, Y. Fu, S. Oyarzun, J. C. Rojas-Sánchez, D. C. Vaz, H. Naganuma, G. Sicoli, J.-P. Attané, M. Jamet, E. Jacquet, J.-M. George, A. Barthélémy, H. Jaffrès, A. Fert, M. Bibes, L. Vila, *Nat. Mater.* **2016**, *15*, 1261.
[11] S. Manipatruni, D. E. Nikonov, C. C. Lin, T. A. Gosavi, H. Liu, B. Prasad, Y. L. Huang, E. Bonturim, R. Ramesh, I. A. Young, *Nature* **2019**, *565*, 35.
[12] A. D. Caviglia, S. Gariglio, N. Reyren, D. Jaccard, T. Schneider, M. Gabay, S. Thiel, G. Hammerl, J. Mannhart, J. M. Triscone, *Nature* **2008**, *456*, 624.
[13] R. Erlandsen, R. T. Dahm, F. Trier, M. Scuderi, E. Di Gennaro, A. Sambri, C. K. Reffeldt Kirchert, N. Pryds, F. M. Granozio, T. S. Jespersen, *Nano Lett.* **2022**, *22*, 4758.
[14] J. S. Lee, Y. W. Xie, H. K. Sato, C. Bell, Y. Hikita, H. Y. Hwang, C. C. Kao, *Nat. Mater.* **2013**, *12*, 703.
[15] D. A. Dikin, M. Mehta, C. W. Bark, C. M. Folkman, C. B. Eom, V. Chandrasekhar, *Phys. Rev. Lett.* **2011**, *107*, 56802.
[16] D. Stornaiuolo, B. Jouault, E. Di Gennaro, A. Sambri, M. D'Antuono, D. Massarotti, F. M. Granozio, R. Di Capua, G. M. De Luca, G. P. Pepe, F. Tafuri, M. Salluzzo, *Phys. Rev. B* **2018**, *98*, 075409.
[17] F. Loder, A. P. Kampf, T. Kopp, *Sci. Rep.* **2015**, *5*, 15302.
[18] A. Jouan, G. Singh, E. Lesne, D. C. Vaz, M. Bibes, A. Barthélémy, C. Ulysse, D. Stornaiuolo, M. Salluzzo, S. Hurand, J. Lesueur, C. Feuillet-Palma, N. Bergeal, *Nat. Electron.* **2020**, *3*, 201.
[19] L. Guo, Y. Yan, R. Xu, J. Li, C. Zeng, *Phys. Rev. Lett.* **2021**, *126*, 057701.

[20] H. Zhang, X. Yan, X. Zhang, S. Wang, C. Xiong, H. Zhang, S. Qi, J. Zhang, F. Han, N. Wu, B. Liu, Y. Chen, B. Shen, J. Sun, *ACS Nano* **2019**, *13*, 609.
[21] C. Liu, X. Yan, D. Jin, Y. Ma, H.-W. Hsiao, Y. Lin, T. M. Bretz-Sullivan, X. Zhou, J. Pearson, B. Fisher, J. S. Jiang, W. Han, J.-M. Zuo, J. Wen, D. D. Fong, J. Sun, H. Zhou, A. Bhattacharya, *Science* **2021**, *371*, 716.
[22] Z. Chen, Z. Liu, Y. Sun, X. Chen, Y. Liu, H. Zhang, H. Li, M. Zhang, S. Hong, T. Ren, C. Zhang, H. Tian, Y. Zhou, J. Sun, Y. Xie, *Phys. Rev. Lett.* **2021**, *126*, 026802.
[23] T. Ren, M. Li, X. Sun, L. Ju, Y. Liu, S. Hong, Y. Sun, Q. Tao, Y. Zhou, Z.-A. Xu, *Sci. Adv.* **2022**, *8*, eabn4273.
[24] Z. Wang, Z. Zhong, X. Hao, S. Gerhold, B. Stoger, M. Schmid, J. Sanchez-Barriga, A. Varykhalov, C. Franchini, K. Held, U. Diebold, *Proc Natl Acad Sci U S A* **2014**, *111*, 3933.
[25] H. W. Jang, D. A. Felker, C. W. Bark, Y. Wang, M. K. Niranjan, C. T. Nelson, Y. Zhang, D. Su, C. M. Folkman, S. H. Baek, S. Lee, K. Janicka, Y. Zhu, X. Q. Pan, D. D. Fong, E. Y. Tsymbal, M. S. Rzchowski, C. B. Eom, *Science* **2011**, *331*, 886.
[26] A. H. Al-Tawhid, J. Kanter, M. Hatefipour, D. P. Kumah, J. Shabani, K. Ahadi, *J. Electron. Mater.* **2022**, *51*, 6305.
[27] X. Hua, F. Meng, Z. Huang, Z. Li, S. Wang, B. Ge, Z. Xiang, X. Chen, *npj Quantum Mater.* **2022**, *7*, 97.
[28] Z. Chen, Y. Liu, H. Zhang, Z. Liu, H. Tian, Y. Sun, M. Zhang, Y. Zhou, J. Sun, Y. Xie, *Science* **2021**, *372*, 721.
[29] N. R. Werthamer, E. Helfand, P. C. Hohenberg, *Phys. Rev.* **1966**, *147*, 295.
[30] G.-H. Cao, Z.-W. Zhu, *Chin. Phys. B* **2018**, *27*, 107401.
[31] Y. Gan, Y. Zhang, D. V. Christensen, N. Pryds, Y. Chen, *Phys. Rev. B* **2019**, *100*, 125134.
[32] H. Liang, L. Cheng, L. Wei, Z. Luo, G. Yu, C. Zeng, Z. Zhang, *Phys. Rev. B* **2015**, *92*, 075309.
[33] G. Bergmann, *Phys. Rep.* **1984**, *107*, 1.
[34] W. Niu, Y.-W. Fang, R. Liu, Z. Wu, Y. Chen, Y. Gan, X. Zhang, C. Zhu, L. Wang, Y. Xu, Y. Pu, Y. Chen, X. Wang, *J. Phys. Chem. Lett.* **2022**, *13*, 2976.
[35] T. Koga, J. Nitta, T. Akazaki, H. Takayanagi, *Phys. Rev. Lett.* **2002**, *89*, 046801.
[36] Y. Zhang, F. Xue, C. Tang, J. Li, L. Liao, L. Li, X. Liu, Y. Yang, C. Song, X. Kou, *ACS Nano* **2020**, *14*, 17396.
[37] Z. Lei, E. Cheah, K. Rubi, M. E. Bal, C. Adam, R. Schott, U. Zeitler, W. Wegscheider, T. Ihn, K. Ensslin, *Phys. Rev. Res.* **2022**, *4*, 013039.
[38] T. S. Suraj, G. J. Omar, H. Jani, M. M. Juvaid, S. Hooda, A. Chaudhuri, A. Rusydi, K. Sethupathi, T. Venkatesan, A. Ariando, M. S. R. Rao, *Phys. Rev. B* **2020**, *102*, 125145.
[39] I. L. Spain, R. O. Dillon, *Carbon* **1976**, *14*, 23.
[40] F. E. Meijer, A. F. Morpurgo, T. M. Klapwijk, J. Nitta, *Phys. Rev. Lett.* **2005**, *94*, 186805.
[41] S. Takasuna, J. Shiogai, S. Matsuzaka, M. Kohda, Y. Oyama, J. Nitta, *Phys. Rev. B* **2017**, *96*, 161303.
[42] A. Joshua, S. Pecker, J. Ruhman, E. Altman, S. Ilani, *Nat. Commun.* **2012**, *3*, 1129.
[43] Y. Gan, D. V. Christensen, Y. Zhang, H. Zhang, D. Krishnan, Z. Zhong, W. Niu, D. J. Carrad, K. Norrman, M. von Soosten, T. S. Jespersen, B. Shen, N. Gauquelin, J. Verbeeck, J. Sun, N. Pryds, Y. Chen, *Adv. Mater.* **2019**, *31*, 1805970.
[44] S. Qi, H. Zhang, J. Zhang, Y. Gan, X. Chen, B. Shen, Y. Chen, Y. Chen, J. Sun, *Adv. Mater. Interfaces* **2022**, *9*, 2200103.
[45] Z. Zhong, A. Tóth, K. Held, *Phys Rev B Condens Matter Mater Phys* **2013**, *87*, 161102(R).
[46] G. Herranz, G. Singh, N. Bergeal, A. Jouan, J. Lesueur, J. Gázquez, M. Varela, M. Scigaj, N. Dix, F. Sánchez, J. Fontcuberta, *Nat. Commun.* **2015**, *6*, 6028.
[47] P. K. Rout, E. Maniv, Y. Dagan, *Phys. Rev. Lett.* **2017**, *119*, 237002.
[48] L. M. Vicente-Arche, J. Bréhin, S. Varotto, M. Cosset-Cheneau, S. Mallik, R. Salazar, P. Noël, D. C. Vaz, F. Trier, S. Bhattacharya, A. Sander, P. Le Fèvre, F. Bertran, G. Saiz, G. Ménard, N. Bergeal, A. Barthélémy, H. Li, C. Lin, D. E. Nikonov, I. A. Young, J. E. Rault, L. Vila, J. Attané, M. Bibes, *Adv. Mater.* **2021**, *33*, 2102102.
[49] N. Kumar, N. Wadehra, R. Tomar, S. K. Shama, Y. Singh, S. Dattagupta, S. Chakraverty, *Adv. Quantum Technol.* **2021**, *4*, 2000081.
[50] G. Singh, A. Jouan, S. Hurand, C. Feuillet-Palma, P. Kumar, A. Dogra, R. Budhani, J. Lesueur, N. Bergeal, *Phys. Rev. B* **2017**, *96*, 24509.
[51] M. Kohda, T. Bergsten, J. Nitta, *J. Phys. Soc. Jpn.* **2008**, *77*, 031008.
[52] J. Nitta, T. Akazaki, H. Takayanagi, T. Enoki, *Phys. Rev. Lett.* **1997**, *78*, 1335.
[53] S. Schmult, M. J. Manfra, A. Punnoose, A. M. Sergent, K. W. Baldwin, R. J. Molnar, *Phys. Rev. B* **2006**, *74*, 033302.
[54] H. C. Koo, J. H. Kwon, J. Eom, J. Chang, S. H. Han, M. Johnson, *Science* **2009**, *325*, 1515.
[55] S. Datta, B. Das, *Appl. Phys. Lett.* **1990**, *56*, 665.
[56] S. Varotto, A. Johansson, B. Göbel, L. M. Vicente-Arche, S. Mallik, J. Bréhin, R. Salazar, F. Bertran, P. L. Fèvre, N. Bergeal, J. Rault, I. Mertig, M. Bibes, *Nat. Commun.* **2022**, *13*, 6165.
[57] R. M. Lutchyn, E. P. A. M. Bakkers, L. P. Kouwenhoven, P. Krogstrup, C. M. Marcus, Y. Oreg, *Nat. Rev. Mater.* **2018**, *3*, 52.
[58] H. Zhang, Y. Yun, X. Zhang, H. Zhang, Y. Ma, X. Yan, F. Wang, G. Li, R. Li, T. Khan, Y. Chen, W. Liu, F. Hu, B. Liu, B. Shen, W. Han, J. Sun, *Phys. Rev. Lett.* **2018**, *121*, 116803.
[59] B. Jäck, Y. Xie, J. Li, S. Jeon, B. A. Bernevig, A. Yazdani, *Science* **2019**, *364*, 1255.
[60] K. V. Shanavas, Z. S. Popović, S. Satpathy, *Phys. Rev. B* **2014**, *90*, 165108.
[61] F. Y. Bruno, S. McKeown Walker, S. Riccò, A. la Torre, Z. Wang, A. Tamai, T. K. Kim, M. Hoesch, M. S. Bahramy, F. Baumberger, *Adv. Electron. Mater.* **2019**, *5*, 1800860.
[62] V. Kumar, N. Ganguli, *Phys. Rev. B* **2022**, *106*, 125127.
[63] G. Venditti, M. E. Temperini, P. Barone, J. Lorenzana, M. N. Gastiasoro, *J. Phys. Mater.* **2023**, *6*, 014007.
[64] P. Krantz, A. Tyner, P. Goswami, V. Chandrasekhar, arXiv: 2209.10534v2, **2022**.
[65] G. Bihlmayer, P. Noël, D. V. Vyalikh, E. V. Chulkov, A. Manchon, *Nat Rev Phys* **2022**, *4*, 642.